Low-ionization structures in planetary nebulae – III. The statistical analysis of physico-chemical parameters and excitation mechanisms

M. Belén Mari[1] ⋆, Stavros Akras[2] and Denise R. Gonçalves[1]

[1]*Observatório do Valongo, Universidade Federal do Rio de Janeiro, Ladeira Pedro Antonio 43, Rio de Janeiro 20080-090, Brazil*
[2]*Institute for Astronomy, Astrophysics, Space Applications and Remote Sensing, National Observatory of Athens, Penteli GR 15236, Greece*

ABSTRACT

Nearly 30 years after the first detailed studies of low-ionization structures (LISs) in planetary nebulae (PNe), we perform a statistical analysis of their physical, chemical and excitation properties, by collecting published data in the literature. The analysis was made through the contrast between LISs and high-ionization structures – rims or shells – for a large sample of PNe, in order to highlight significant differences between these structures. Our motivation was to find robust results based on the largest sample of LISs gathered so far. (i) Indeed, LISs have lower electron densities (N_e[S II]) than the rims/shells. (ii) The nitrogen electron temperatures (T_e[N II]) are similar between the two groups, while a bimodal distribution is observed for the T_e based on [O III] of the rims/shells, although the high- and low-ionization structures have T_e[O III] of similar median values. (iii) No significant variations are observed in total abundances of He, N, O, Ne, Ar, Cl and S between the two groups. (iv) Through the analysis of several diagnostic diagrams, LISs are separated from rims/shells in terms of excitation. From two large grids of photoionization and shock models, we show that there is an important overlap between both mechanisms, particularly when low-ionization line-ratios are concerned. We found a good tracer of high-velocity shocks, as well as an indicator of high- and low-velocity shocks that depends on temperature-sensitive line ratios. In conclusion, both excitation mechanisms could be present, however shocks cannot be the main source of excitation for most of the LISs of PNe.

Key words: ISM: kinematics and dynamics – ISM: jets and outflows – planetary nebulae: general

1 INTRODUCTION

This is the third of a series of papers carrying out an optical spectroscopic study of low-ionization structures (LISs; Gonçalves et al. 2001) and their host planetary nebulae (PNe). In Paper I (Akras & Gonçalves 2016) and II (Mari, Gonçalves & Akras 2023), the spectroscopic study of 5 and 6 PNe, respectively, were presented. These papers completed the analysis of the sample whose initial data were published in Gonçalves et al. (2003, 2004, 2009). The spectroscopic analysis was carried out for two different groups of nebular components: the high-ionization ones – rims or shells – and low-ionization structures.

Overall, PNe have large-scale structures such as rims and shells, bright in the light of hydrogen and helium recombination lines, as well as in the forbidden [O III] lines. The formation of the rims and shells in PNe is relatively well understood (see Balick & Frank 2002, for a review). On somewhat smaller scales, they can present LISs, visible primarily in low-ionization species such as [N II], [S II], [O II] and also [O I] (e.g. Balick et al. 1993; Corradi et al. 1996; Gonçalves et al. 2001). The origin of these small-scale structures still remain an open question in the field of photoionized nebula. Several studies have been performed since their earlier report (Balick 1987), using either imaging (Balick 1987; Schwarz et al. 1992; Manchado et al. 1996; Corradi et al. 1996; Balick et al. 1998; Górny et al. 1999) or

spectroscopic data (Balick et al. 1994; Hajian et al. 1997; Gonçalves et al. 2003, 2004, 2009; Akras & Gonçalves 2016; Danehkar et al. 2016; Ali & Dopita 2017; Monreal-Ibero & Walsh 2020; Miranda et al. 2021; Akras et al. 2022; Mari et al. 2023). These spectroscopic studies about LISs and their host PNe came, independently, to the conclusion that LISs are characterized by lower – or at most equal – electron density (N_e) than the surrounding gas (rims and shells), while the electron temperature (T_e) and the chemical composition of rims, shells and LISs appear to be the same.

Such low N_e in LISs contradicts the formation mechanisms proposed to explain these micro-structures, as most of the theoretical reasoning and models consider them as dense structures moving in a tenuous environment (Steffen et al. 2001; Raga et al. 2008; Balick et al. 2020). The fact that molecular hydrogen (H_2) emission from the cometary knots in the Helix nebula (Matsuura et al. 2009) was known for a while led Gonçalves and collaborators to proposed that LISs, other than the cometary knots, may also contain molecular gas and dust (Gonçalves et al. 2009). Recent studies focused on the near-infrared ro-vibrational H_2 line centred at 2.12 μm have unveiled the H_2 counterpart of several LISs (Fang et al. 2015; Akras et al. 2017; Fang et al. 2018; Akras et al. 2020c). These H_2 condensations have a size around 2-5×10^{16} cm, while the host PNe are relatively young, <2000 years (Akras et al. 2020a). These findings imply the presence of high-density gas, enough to shield the molecular matter from the central star UV radiation and prevent its dissociation, as predicted by LISs' formation models (e.g. Balick et al. 2020).

The dominant excitation mechanism in LISs can be either photoionization from the UV radiation of the central stars or shock interaction with the other nebular components or the circumstellar medium. Both mechanisms are supported by the enhanced low-ionization line ratios (e.g. [N II] /Hα, [S II]/Hα, [O I]/Hα, etc.) observed in LISs (using diagnostic techniques as, e.g. Sabbadin et al. 1977; Raga et al. 2008).

In the context of an overall view of LISs in PNe, publicly available spectroscopic results, from the literature, for PNe with LISs, were gathered with the intention of carrying out the first statistical analysis of their physical, chemical and excitation mechanisms, to identify potential patterns and trends.

The paper is organized as follows: the data sample gathered from the literature and their visualization are presented in section 2. The results of our statistical analysis are presented in Section 3. In Section 4, we discuss the predictions from photoionization and shocks models. Diagnostic diagrams for the separation of photoionized and shocks-heated gases are discussed. Overall discussions and conclusions appear in Section 5 and 6, respectively.

2 DATA SAMPLE AND VISUALIZATION

A statistical study of the physical, chemical and excitation mechanisms of PNe and their LISs is missing. To solve this problem, in this work, we have gathered spectroscopic information for LISs and their host PNe available in the literature. Table 1 lists these objects and the references from which we collected the data. In total, our sample consists of 33 PNe, with 88 Rims/Shells and 104 LISs, the largest and most complete sample analysed this far. LISs refers to – generally small – structures, bright in low-ionization lines, with the appearance of knots or filaments. Rims and shells, on the other hand, are of larger scales, much higher in ionization and result from the interacting AGB/post-AGB stellar winds, photoionized by the central star radiation (e.g. Balick 1987).

It is important to point out the fact that, since the data collected were published over ~30 years by different authors, it is not homogeneous in terms of atomic data, excitation curves, ionization correction factors for total abundances, etc. The line ratios (already corrected by extinction), as well as the physico-chemical properties, were taken without further manipulation. The exception are Gonçalves et al. (2003, 2004, 2009) objects, for which we applied the c_β correction using their reported values of extinction.

An integrated way to visualize and explore this sample is through the use of *violinplots* in conjunction with the statistical analysis of the *boxplots*, embedded in the former plots. This type of representation allows for different shapes of the distributions and makes clear the presence of clustering, such as bimodalities (see Appendix A), as they use a kernel density distribution. To detect significant differences between the samples, the use of *notches* is of great help, as they represent the 95% confidence interval (CI) for the median (Hintze & Nelson 1998). When the notches of the distributions of two groups do not overlap, we can safely conclude that the samples indeed differ (Chambers et al. 2017). Considering that the aim of this work is to find different trends between Rims/Shells and LISs in PNe, we work with violinplots throughout this study.

3 RESULTS

Here, we perform a statistical analysis of the N$_e$ (Section 3.1) and T$_e$ (Section 3.2) obtained from the [S II], [N II] and [O III] diag-

Table 1. PNe with LISs, from the literature.

Name	Rims/Shells	LISs	References
NGC 6543[†]	2	1	Balick et al. (1994)
NGC 6826	1	1	Balick et al. (1994)
NGC 7009[†]	2	1	Balick et al. (1994)
Hb 4	2	2	Hajian et al. (1997)
IC 4634[†]	3	2	Hajian et al. (1997)
NGC 6369	2	2	Hajian et al. (1997)
NGC 7354[†]	4	2	Hajian et al. (1997)
M 2-48	1	2	López-Martín et al. (2002)
NGC 7009[†]	2	6	Gonçalves et al. (2003)
K 4-47	1	2	Gonçalves et al. (2004)
NGC 7662[†]	1	6	Perinotto et al. (2004)
IC 4634[†]	3	2	Guerrero et al. (2008)
He 1-1	1	2	Gonçalves et al. (2009)
IC 2149	1	2	Gonçalves et al. (2009)
KjPn 8	-	2	Gonçalves et al. (2009)
NGC 7662[†]	7	2	Gonçalves et al. (2009)
NGC 7354[†]	11	10	Contreras et al. (2010)
The Necklace	1	1	Corradi et al. (2011)
ETHOS 1	2	3	Miszalski et al. (2011)
NGC 3242	2	5	Monteiro et al. (2013)
Hu 1-2	2	1	Fang et al. (2015)
IC 4846	1	2	Akras & Gonçalves (2016)
Wray 17-1	6	6	Akras & Gonçalves (2016)
K 1-2	-	5	Akras & Gonçalves (2016)
NGC 6891	6	2	Akras & Gonçalves (2016)
NGC 6572	2	4	Akras & Gonçalves (2016)
M 2-42	1	2	Danehkar et al. (2016)
NGC 5307	-	3	Ali & Dopita (2017)
IC 2553	-	2	Ali & Dopita (2017)
PB 6	-	1	Ali & Dopita (2017)
NGC 3132	-	2	Monreal-Ibero & Walsh (2020)
IRAS 18061–2505	2	2	Miranda et al. (2021)
IC 4593	4	3	Mari et al. (2023)
Hen 2-186	1	2	Mari et al. (2023)
Hen 2-429	1	2	Mari et al. (2023)
NGC 3918	3	5	Mari et al. (2023)
NGC 6543[†]	8	2	Mari et al. (2023)
NGC 6905	2	2	Mari et al. (2023)
Total	88	104	

Note: [†] These PNe, NGC 6543, NGC 7009, IC 4634, NGC 7354 and NGC 7662, are repeated because the structures studied in each work are, in general, different.

nostic lines. Then a similar analysis is carried out for the chemical abundances of the host PNe and LISs (Section 3.3). We finish the presentation of the results exploring a few characteristic emission-line ratios, which concern the probable excitation mechanism present in the different structures of the PNe studied (Section 3.4).

3.1 Electron density

In the top panels of Figure 1, we present the N$_e$ for the two subsets of Rims/Shells (cyan) and LISs (green). The size of the thick vertical black lines at the centre of the violinplots represent the interquartile range (IQR), whereas the white dot corresponds to the median value of each data set. The distributions are found to be similar in both groups, with comparable widths. As expected from previous studies, the group of LISs (sample size equal to 98) clearly shows a peak at lower densities compared to the group of Rims/Shells (80), whereas
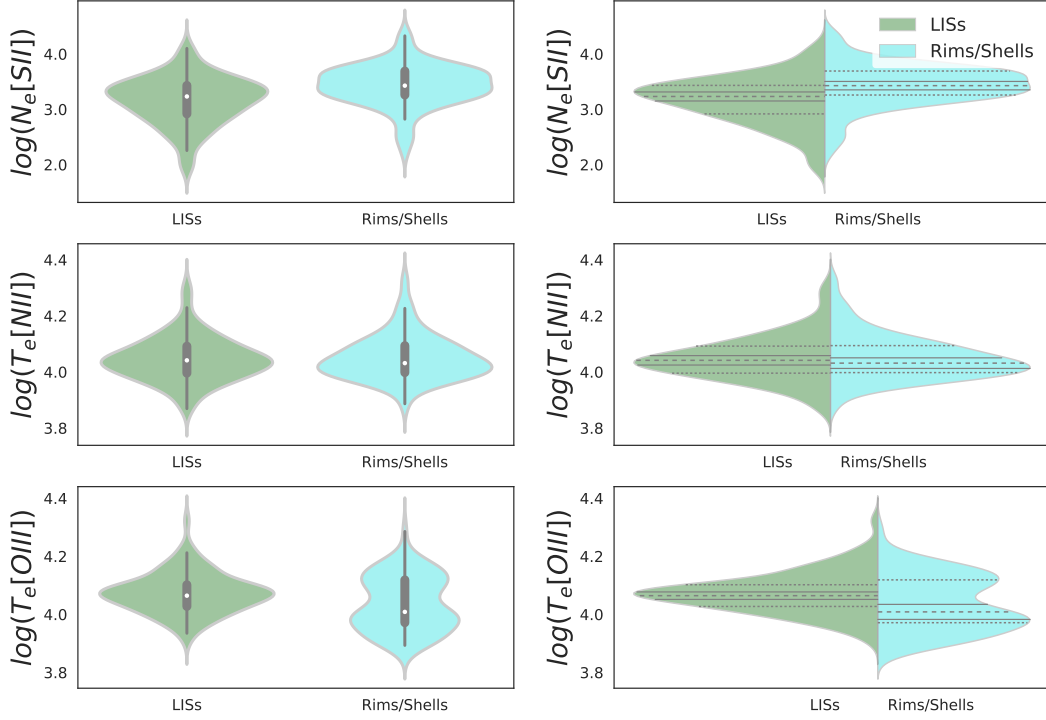
Figure 1. Violinplots showing the electron temperature and density for the two groups: Rims/Shells (in cyan) and LISs (in green). *Left panels*: comparison between the two components with violinplots with boxplots inside. *Right panels*: comparison between LISs and Rims/Shells using split violinplots with the median (Q2), 25th and 75th quartiles (Q1 and Q3) shown by dashed and dotted lines, respectively, and the notches represented by solid lines.

Table 2. Group properties for the samples of Rims/Shells and LISs. The notches correspond to the approximated 95 per cent CIs. The last two rows show the number of outliers and sample size, respectively.

	$\log(N_e[\text{S II}])$		$\log(T_e[\text{N II}])$		$\log(T_e[\text{O III}])$	
	Rims/Shells	LISs	Rims/Shells	LISs	Rims/Shells	LISs
Mean	3.4308	3.1596	4.0498	4.0447	4.0344	4.0726
Median	3.4249	3.2326	4.0314	4.0414	4.0086	4.0645
Lower notch	3.3477	3.1510	4.0125	4.0246	3.9826	4.0516
Upper notch	3.5021	3.3143	4.0503	4.0582	4.0346	4.0773
IQR	0.4370	0.5149	0.0962	0.0964	0.1470	0.0747
Q1	3.2576	2.9177	3.9976	3.9956	3.9696	4.0273
Q3	3.6946	3.4326	4.0938	4.0920	4.1166	4.1021
#Outliers	4	3	2	2	0	3
#Sample	79	98	64	81	79	83

there is a small number of LISs, Rims and Shells, which exhibit N_e close to or even higher than 10^4 cm^{-3}. Likewise, there is a small number of Rims/Shells with N_e lower than $10^{2.5}$ cm^{-3}. The wing of the distribution may indicate measurements with high uncertainties and outliers (see Table 2).

In Table 2, we list the statistical quantifies for both groups. The median values of $\log(N_e)$ are 3.42 (~2700 cm^{-3}) and 3.23 (~1700 cm^{-3}) for the Rims/Shells and LISs, respectively. Taking into account the lower and upper notches, it is clear that there is no overlap between the two groups, with a ~95% of CI. Therefore, LISs represent a statistically different sample than the Rims/Shells in terms of electron density.

3.2 Electron temperature

The middle panels of Fig. 1 show the T_e from the [N II] emission-lines. The T_e[N II] distribution is nearly similar for both groups. The median value of $\log(T_e[\text{N II}])$ is almost the same for LISs and Rims/Shells, being 4.04 (~11000 K) and 4.03 (~10700 K), respectively. The upper and lower notches of the two type of structures (see Table 2) allow the clear conclusion that both groups are identical in terms of T_e[N II]. On the other hand, looking at the violinplots of T_e[O III] (bottom-left panel in Fig. 1) we note that the group of Rims/Shells displays a bimodal distribution with peaks at ~3.97 and ~4.12, while LISs show a nearly bell-shell distribution with a peak at ~4.07. Scrutinizing the results of $\log(T_e[\text{O III}])$, we also notice that the median value of Rims/Shells is lower than the values obtained from LISs (see the white dots Fig. 1, in bottom-left panel). In particular, LISs have a median $\log(T_e[\text{O III}])$ value of 4.06 (~11500 K)

and Rims/Shells of 4.01 (~10200 K). This difference is significant, and we could argue that the two groups are statistically different in terms of T_e[O III] as there is no overlap of their notches (see Table 2). However, we should also note that the peak of $log(T_e$[O III]) for the LISs is similar to the valley of the bimodality present in the distribution of the Rims/Shells – whose peaks approximately coincide with the Q1 and Q3 of its distribution. This result shows that a significant number of LISs has higher T_e[O III] than Rims/Shells, which could be interpreted as an extra excitation mechanism in LISs.

The right panel of Fig. 1 illustrate the *split* distributions (i.e. one-half of the violinplots) of N_e and T_e side-by-side, for a direct comparison. The median, notches and IQR parameters for the two groups, as well as the size of the samples, are listed in Table 2. The straightforward results from the table and plots is that LISs and Rims/Shells have different properties in terms of N_e[S II] and T_e[O III] and behave similarly when T_e[N II] is concerned.

3.3 Abundances

Regarding the total abundance of N, Ar, S, Ne and Cl, in Fig. 2 we present different abundance ratio combinations (see also, Henry 1990). From these correlations we do not find any specific locus for LISs or Rims/Shells which would indicate chemical inhomogeneities, but some structures notably distant from the linear correlation – marked with solid arrows – are identified. A particular example is K 4-47, which is composed of a compact high-ionization core and a pair of LISs with strong emission from low-ionization species, both studied by Gonçalves et al. (2004). A strong H_2 emission is associated to the LISs (Akras et al. 2017). Relative to the rest of PNe and LISs in the sample, this nebula shows significantly higher N/O, S/O and Ne/O abundance ratios. A second example is the Rims/Shells in Wray 17-1 (Akras & Gonçalves 2016, named *inner NEBs*) for which a higher Ar/O ratio is found. A third example is the knots (or LISs) in the K 1-2 (Akras & Gonçalves 2016) for which a higher Ar/O ratio is also found. For this last PN, it has been found that the central star is a post-CE close binary system (Exter et al. 2003). Note that these three PNe display a highly collimated jet-like structure with knots present at the end of them (Corradi et al. 1996; Gonçalves et al. 2004).

Fig. 2 also includes the linear fit of the correlations, with the gray filled area corresponding to the uncertainties. The structures that deviated significantly from bulk, marked with solid arrows, were excluded from the linear fitting. In Table 4 we list the slope (*a*), intercept (*b*), goodness-of-fit (R^2) and the number of the data points considered, without LISs. These structures were eliminated with the intention to look for potential deviations due to this specific group. In order to compare the distributions between the two groups of PN structures, the top and right side of each of the panels in Fig. 2 show the split violinplots of the abundance ratio correlations. In general, there are no major differences between the distributions nor between their median values (see Table 3). Moreover, also taking into account the upper and lower notches of the correlations, we conclude that LISs, rims and shells are similar in terms of total elemental abundances. There are a few structures that are outliers from both violinplots of each panel – that were not marked to avoid confusion. Although the latter outliers correspond to values that deviate significantly from the distributions of each group, it can be observed that, in general, they do not deviate from the linear correlation. K 4-47, for which the total abundances of He, O, N, Ne and S were studied by Gonçalves et al. (2004) is the only PN that is outlier for all the abundances correlations. As pointed out by the authors, neither the core nor the LISs of this PN can be explained

by pure photoionization, and therefore its abundance ratios are not reliable.

For the widely studied log(N/H) versus log(N/O) diagram, we determine $log(N/O) = (0.73 \pm 0.03) \times [12 + log(N/H)] - (6.38 \pm 0.23)$, $R^2 = 0.82$, very close to the previous result reported by Akras & Gonçalves (2016) $(log(N/O) = 0.74 \times [12 + log(N/H)] - 6.50$; with $R^2 = 0.88$) considering only five PNe though. García-Rojas et al. (2013) also determined practically the same relation $(log(N/O) = 0.73 \times [12 + log(N/H)] - 6.50$; with $R^2 = 0.86$) but for a sample of PNe with [WR] and *wels* CSPNe. According to García-Rojas et al. (2013), this linear relationship indicates that N-enrichment in PNe occurs independently of the O abundance, being mainly due to the CN-cycle – where N increases at the expense of C – and not to the ON-cycle. This last one would reduce the O/H ratio in low-metallicity PNe with progenitor stars higher than $\sim 2M_\odot$, which can be observed for $log(O/H) + 12 \leq 8$ (Maciel et al. 2017). In the upper left panel of Fig. 2 it can be seen that this value is achieved for three nebulae corresponding to K 4-47, K 1-2 and Wray 17-1. This idea is reinforced just for one of those PNe by looking at the upper right panel, in which the log(N/O) is lower than 0.5 for all structures, except the LISs in K 4-47. According to Cavichia et al. (2010, 2017), PNe with log(N/O)~0.5 could be originated from massive stars, i.e., the higher N/O ratio, the more massive progenitor stars.

The result from this work is, considering the errors, similar to the previously published ones. Nevertheless, for comparison purposes, in Table 4 we list the parameters of the linear fitting, excluding the LISs. Globally, the correlation with and without LISs do not vary strongly – variations are at most of ~6% on slope and intercept – as highlighted by the R^2 values, except for Ne/O. Remembering that R^2 ranges from 0 to 1 – the higher the value, the better the fit – the table shows that without the LISs, the coefficients are closer to 1.

Altogether, these abundance ratio correlations are suggesting that Ar, S, Ne and Cl vary in lockstep with O, which means that the former element's nucleosynthesis during the evolution of the progenitor star, as compared to the latter, are small – or even negligible (Cavichia et al. 2010; Maciel et al. 2017).

3.4 Excitation mechanism

Aiming to understand the nature of the nebula S176, Sabbadin, Minello & Bianchini (1977) (hereafter SMB) introduced a diagnostic diagram (DD), based on the Hα/[N II] $\lambda\lambda6548,6584$ and Hα/[S II] $\lambda\lambda6716,6731$ line ratios, to distinguish PNe from HII regions and supernova remnants (SNRs). The position of these nebulae is distinctive because of the excitation mechanism and physico-chemical properties responsible for the production of the emission-line involved. Riesgo & López (2006) used a larger sample of PNe and provided a more restrict region through a density probability ellipse, on the same DD (see also Frew & Parker 2010; Sabin et al. 2013; Akras et al. 2020b).

In Fig. 3 we display SMB for our sample of PNe, Rims/Shells and LISs[1]. The disparity in the Hα/[N II] and Hα/[S II] line ratios between LISs and Rims/Shells is evident in this DD. Most LISs, by definition characterized by enhanced [N II] and [S II] lines relative to Hα, lie in the bottom-left half of the density ellipse with

---

[1] It is important to note that the diagrams under discussion were developed using the integrated emission of many PNe. Here, as first proposed by Gonçalves et al. (2003), they are used for different components of the same PN, in a spatially resolved fashion. The differences of integrated and spatially resolved analysis are also discussed in Akras et al. (2020b, 2022)
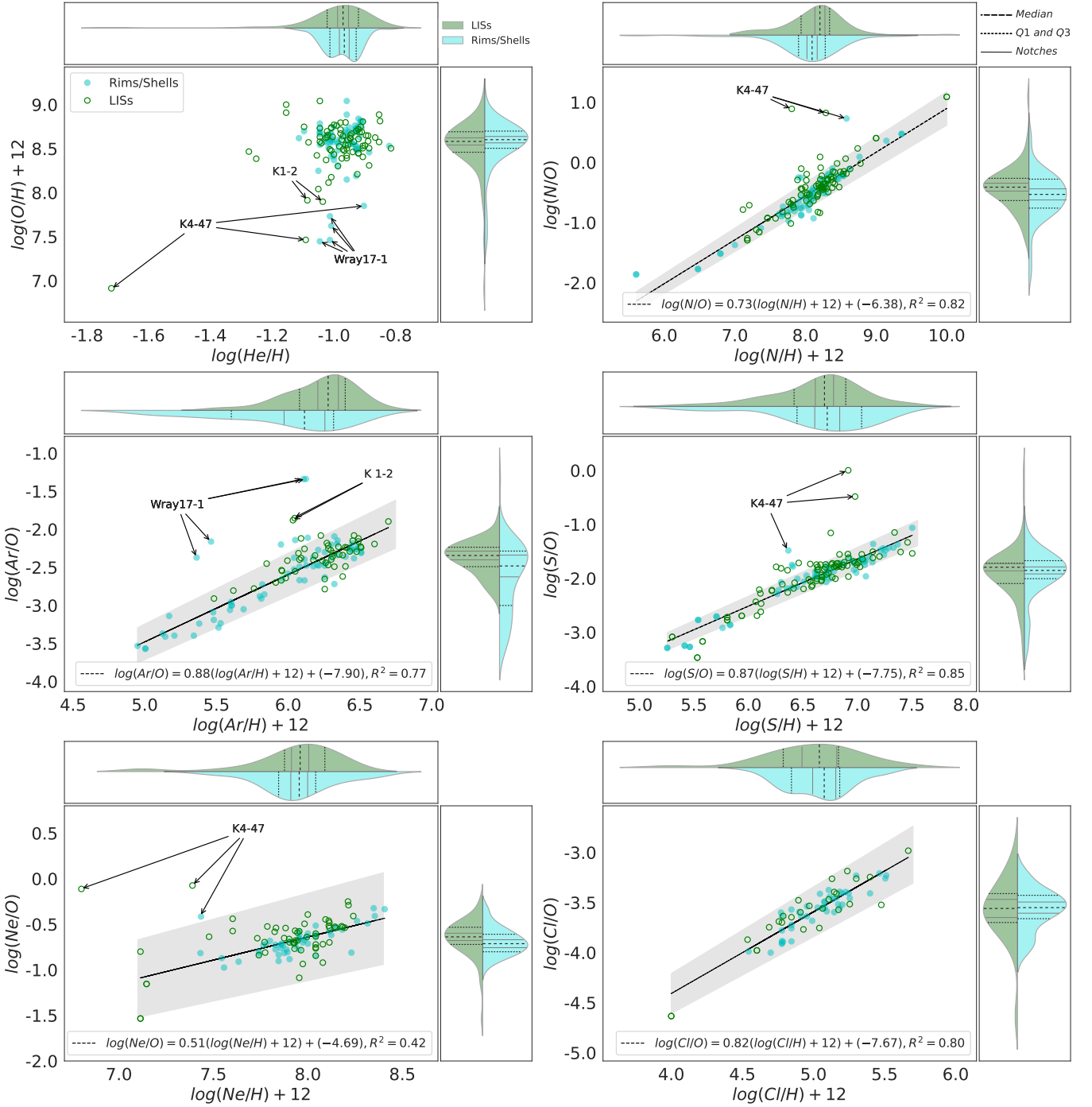
Figure 2. Correlations between total abundances using both components in the sample (Rims/Shells and LISs). Below each plot, the trend line with its goodness-of-fit (R^2) per pair of elements is listed. The gray filled area represents the uncertainty of the regression line. Above and to the right of each panel, the split violinplots comparing Rims/Shells and LISs groups.

$\log(\text{H}\alpha/[\text{N \textsc{ii}}]) < 1.0$ and $\log(\text{H}\alpha/[\text{S \textsc{ii}}]) < 1.8$. On the other hand, the vast majority of the Rims/Shells are distributed in the top-right of the PNe locus in the diagram. This becomes even more evident when looking at the split violinplots corresponding to each of the axes. Taking into account the upper and lower notches (see Table 5) it is evident that the two groups are statistically different. This separation between LISs and Rims/Shells is attributed to the difference in the ionization state of these nebular components (Akras et al. 2020c),

which can also be interpreted as excitation stratification (Gonçalves et al. 2003).

Two other DDs were proposed by Baldwin, Phillips & Terlevich (1981) (hereafter BPT) to explore the excitation mechanisms in galaxies. The corresponding BPT diagrams for PNe, H\textsc{ii} regions and SNRs were discussed by Frew & Parker (2010). Fig. 4 shows the distributions of LISs and Rims/Shells in the BPT diagrams, together with their violinplots. Some particular cases that deviate from the bulk of
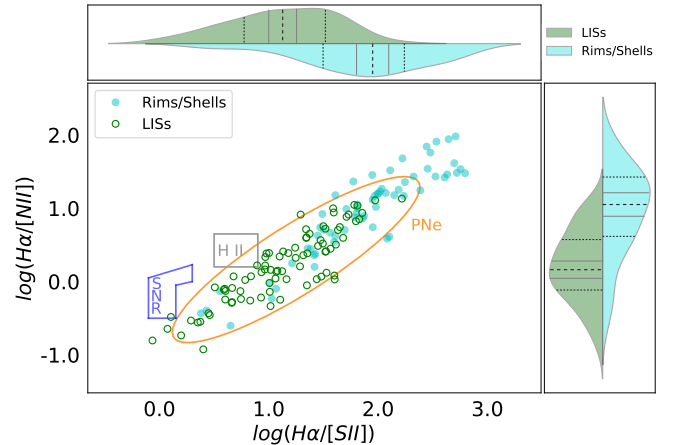
Table 3. Same as Table 2, but for abundances.

| | log(He/H) | | log(O/H)+12 | | log(N/O) | | log(N/H)+12 | |
	Rims/Shells	LISs	Rims/Shells	LISs	Rims/Shells	LISs	Rims/Shells	LISs
Mean	-0.9741	-0.9876	8.5421	8.5309	-0.5625	-0.4335	8.0387	8.1322
Median	-0.9666	-0.9706	8.6021	8.5821	-0.5301	-0.4096	8.0934	8.2041
Lower notch	-0.9824	-0.9884	8.5657	8.5412	-0.6224	-0.4749	8.0209	8.1329
Upper notch	-0.9507	-0.9528	8.6384	8.6229	-0.4377	-0.3443	8.1660	8.2753
IQR	0.0851	0.1015	0.1950	0.2326	0.4814	0.3697	0.3782	0.4030
Q1	-1.0132	-1.0223	8.5044	8.4594	-0.7583	-0.6324	7.9015	7.9380
Q3	-0.9281	-0.9208	8.6994	8.6920	-0.2768	-0.2627	8.2796	8.3410
#Outliers	0	3	8	6	4	4	6	7
#Sample	71	80	71	80	67	79	67	79

| | log(Ar/O) | | log(Ar/H)+12 | | log(S/O) | | log(S/H)+12 | |
	Rims/Shells	LISs	Rims/Shells	LISs	Rims/Shells	LISs	Rims/Shells	LISs
Mean	-2.6381	-2.3811	5.9654	6.2245	-1.9413	-1.9516	6.6829	6.6241
Median	-2.4819	-2.3440	6.1139	6.2788	-1.8646	-1.8129	6.7243	6.6776
Lower notch	-2.6244	-2.4012	5.9717	6.2073	-1.9291	-1.8826	6.6092	6.5957
Upper notch	-2.3393	-2.2867	6.2562	6.3502	-1.8001	-1.7433	6.8394	6.7595
IQR	0.7149	0.2552	0.7132	0.3188	0.3314	0.3893	0.5911	0.4578
Q1	-3.0008	-2.4907	5.6037	6.0792	-2.0076	-2.1099	6.4502	6.4150
Q3	-2.2859	-2.2355	6.3169	6.3979	-1.6762	-1.7205	7.0414	6.8727
#Outliers	0	1	0	1	9	6	4	3
#Sample	62	49	62	49	65	77	65	77

| | log(Ne/O) | | log(Ne/H)+12 | | log(Cl/O) | | log(Cl/H)+12 | |
	Rims/Shells	LISs	Rims/Shells	LISs	Rims/Shells	LISs	Rims/Shells	LISs
Mean	-0.6894	-0.6548	7.9519	7.9248	-3.5712	-3.5761	5.0412	4.9944
Median	-0.7129	-0.6383	7.9542	7.9590	-3.5504	-3.5588	5.0755	5.0414
Lower notch	-0.7565	-0.6785	7.9098	7.9134	-3.6062	-3.6494	4.9942	4.9194
Upper notch	-0.6693	-0.5980	7.9987	8.0046	-3.4946	-3.4682	5.1569	5.1634
IQR	0.1923	0.1884	0.1963	0.2135	0.2332	0.2886	0.3396	0.3886
Q1	-0.8017	-0.7212	7.8451	7.8764	-3.6607	-3.6990	4.8451	4.7875
Q3	-0.6094	-0.5328	8.0414	8.0899	-3.4275	-3.4103	5.1847	5.1761
#Outliers	0	3	5	4	0	1	0	1
#Sample	48	54	48	54	43	25	43	25

Table 4. Slope, intercept, goodness-of-fit and number of the sample of the fitted trend lines for correlations between different abundance ratios without the LISs. In parentheses, the values for the correlations using the two groups (Rims/Shells and LISs) are specified.

	a	b	R^2	#Sample
log(N/O)	0.71±0.03 (0.73±0.03)	-6.28±0.27 (-6.38±0.23)	0.88 (0.82)	67 (146)
log(Ar/O)	0.93±0.06 (0.88±0.05)	-8.17±0.37 (-7.90±0.28)	0.79 (0.77)	62 (111)
log(S/O)	0.88±0.03 (0.87±0.03)	-7.81±0.23 (-7.75±0.20)	0.91 (0.85)	65 (142)
log(Ne/O)	0.57±0.06 (0.51±0.06)	-5.21±0.48 (-4.69±0.48)	0.66 (0.42)	48 (102)
log(Cl/O)	0.81±0.06 (0.82±0.05)	-7.65±0.32 (-7.67±0.25)	0.80 (0.80)	43 (68)

Figure 3. Hα/[N II] 6548+6584 versus Hα/[S II] 6716+6731 diagnostic diagram (Sabbadin et al. 1977) with the density ellipse of probability 0.85 from Riesgo & López (2006).

the data with apparent enhanced [S II]/Hα and [N II]/Hα ratios are indicated with arrows. Two cyan data points (Rims/Shells) exhibit the lowest [O III]/Hβ ratio and correspond to the lobes of the water maser emitting PN (H$_2$O-PN) IRAS 18061–2505 (Miranda et al. 2021), while its [S II]/Hα and [N II]/Hα ratios are significantly high.

Two LISs of this young nebula are described by stronger [O III] λ5007 emission and comparable [S II]/Hα and [N II]/Hα ratios. Miranda et al. (2021) argued that the optical spectra of the bow-shock struc-

tures (LISs for our definition) of H_2O-PN are attributed to shock interactions, while the photoionization dominates the spectra of the lobes (Rims/Shells **here**), if the mass of the progenitor star is $\gtrsim 3M_\odot$. Two LISs with high [S II]/Hα and [N II]/Hα ratios are also found in KjPn 8 (Gonçalves et al. 2009). These authors concluded that both LISs are consistent with both shock- and photoionization playing a role in the measured emission line ratios.

Another two LISs, from the unusual PN K 4-47 (Gonçalves et al. 2004), are also characterized by high [S II]/Hα and [N II]/Hα ratios. Based on the prediction from shock modelling, both LISs are shock dominated. The high H_2 (1-0)/(2-1) ratio measured for these structures is also attributed to shock-heated gas (Lumsden et al. 2001; Akras et al. 2017), but the hypothesis of a high density gas ($>10^4$ cm^{-3}) illuminated by an intense UV radiation field has not been ruled out yet. Two more LISs, from M 2-48, exhibit high [N II]/Hα and [S II]/Hα ratios. This nebula with its multiple knots (LISs) was studied by (López-Martín et al. 2002), who conclude that shock excitation is contributing to the spectra of both LISs analysed in contrast to the central region, which is radiatively excited. Finally, the two arc-like structures found in NGC 3132 (Monreal-Ibero & Walsh 2020) also exhibit high [S II]/Hα and [N II]/Hα ratios. IRAC images from *Spitzer* have revealed mid-IR emission at the position of these arc-like structures, likely from H_2 lines (Hora et al. 2004). Early release images from JWST confirmed the presence of H_2 emission throughout this nebula (De Marco et al. 2022). Although, it is likely that unidentified infrared emission bands (UIBs) detected in NGC 3132 (Mata et al. 2016) also contribute to the *Spitzer's* images.

From the statistical point of view, LISs and Rims/Shells subsets are different groups in terms of the [N II]/Hα and [S II]/Hα line ratios. The aforementioned LISs are characterized by lower [O III]/Hβ ratios ($\lesssim 0.5$) relative to the main bulk of data points (see Table 5) and significantly higher [N II]/Hα and [S II]/Hα line ratios. We thus argue that the shock-heating process is likely active in these particular cases, which are prone to further studies. Note that all these LISs exhibit [S II]/Hα>0.4, a strong tracer of shocks (e.g. Leonidaki et al. 2013; Kopsacheili et al. 2020). The shock velocity in these cases should be ≤ 100 km s^{-1}.

To further explore the ionization state of the PNe in our sample, we also built the [O II] $\lambda 3727$/[O III] $\lambda 5007$ versus [O I] $\lambda 6300$/Hα diagram for both LISs and Rims/Shells subsets (Fig. 5). The advantage of this DD is that only one chemical element in used, unlike the **rest** DDs. A clear separation between LISs and Rims/Shells is observed. The former occupy the top-right corner in the plot, with high [O II] $\lambda 3727$/[O III] $\lambda 5007$ and [O I] $\lambda 6300$/Hα line ratios, while Rims/Shells are found to be concentrated in the bottom-left corner with lower line ratios. The bottom panel in Fig. 5 illustrates the same plot with the confidence ellipses of 1, 2, and 3σ. Note that the two groups display different slopes, which indicate an important alteration of the ionization state between the two components. Their violinplots and statistical parameters (Table 5) make it clear that LISs and Rims/Shells are certainly different samples. Nonetheless, it is important to note that, because the [O I] $\lambda 6300$ is not always detectable, the number of data points in Fig. 5 is lower than in the previous DDs – having 44 LISs and 24 Rims/Shells – so the results should be treated with caution.

One can see that there are LISs into the locus of Rims/Shells and vice versa. This could be interpreted as a transition zone. Particularly, three LISs in NGC 7009 that corresponding to the K2 and K3 knots (Gonçalves et al. 2003) and western ansae (Balick et al. 1994) have lower [O II] $\lambda 3727$/[O III] $\lambda 5007$ ratio relative to the bulk of LISs. A similar behaviour is also observed for the northern ansae in NGC 6543 (Balick et al. 1994), the north-
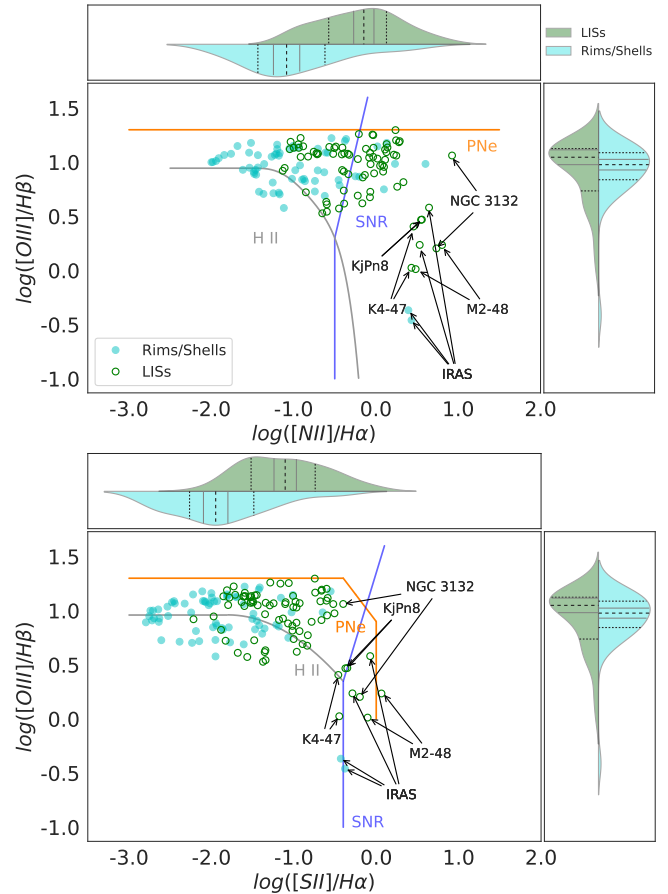

Figure 4. *Top panel:* [N II] 6548+6584/Hα versus [O III] 5007/Hβ BPT diagnostic diagram with the regions of PNe, H II regions and SNRs (Frew & Parker 2010; Sabin et al. 2013). *Lower panel:* [S II] 6716+6731/Hα versus [O III] 5007/Hβ BPT diagram.

west knot2 in NGC 6905 and the B' LIS in NGC 3918, contrary to the C-LIS in IC 4593 (Mari et al. 2023) and southeast ansae NGC 6826 which are characterized by low [O I]$\lambda 6300$/Hα ratio and high [O II] $\lambda 3727$/[O III] $\lambda 5007$. On the other hand, there are three cases of Rims/Shells (corresponding to Hen 2-186, Hen 2-429 and K 4-47) with high [O II] $\lambda 3727$/[O III] $\lambda 5007$ and [O I]$\lambda 6300$/Hα ratios placed into the regime of LISs. Hen 2-186 is a poorly studied southern PN and, according to Guerrero et al. (2020), it belongs to a limited group of nebulae whose jets have velocities exceeding 100 kms^{-1}. Hen 2-429 is also a PN that belong in PNe with embedded jets and finally, K 4-47 with a collimated structure and a pair of shock-heated LISs. While these three last examples are Rims/Shells and do not include the jets, filaments or knots of low-ionization, they may also contain some shock excitation contribution. Taking into account that LISs and Rims/Shells occupy two separate regions with different slopes, we conclude that the ionization state of the nebular gas in the two groups is certainly different.

4 PHOTOIONIZATION VERSUS SHOCK MODEL PREDICTIONS

The disentanglement of UV photo-heated and shock-heated gases in the SMB and BPT DDs (Figs 3 and 4) is still not well-defined, as both mechanisms yield comparable line ratios. The availability of

Table 5. Group properties for the samples of Rims/Shells and LISs for log(Hα/[S ɪɪ]6717+6731), log(Hα/[N ɪɪ]6548+6584), log([O ɪɪɪ]5007/Hβ), log([O ɪ]6300/Hα and log([O ɪɪ]3727/[O ɪɪɪ]5007). The notches correspond to the approximated 95 per cent CIs **(see Appendix A)**. The last two rows show the number of outliers and sample size, respectively.

	log(Hα/[S ɪɪ])		log(Hα/[N ɪɪ])		log([O ɪɪɪ]/Hβ)		log([O ɪ]/Hα)		log([O ɪɪ]/[O ɪɪɪ])	
	Rims/Shells	LISs	Rims/Shells	LISs	Rims/Shells	LISs	Rims/Shells	LISs	Rims/Shells	LISs
Mean	1.8680	1.1248	0.9510	0.2122	0.9221	0.9163	-2.2603	-1.3055	-1.3525	-0.7563
Median	1.9501	1.1271	1.0517	0.1623	0.9718	1.0461	-1.9931	-1.1894	-1.3858	-0.7311
Lower notch	1.8031	0.9997	0.8915	0.0443	0.9222	0.9775	-2.3557	-1.3366	-1.5326	-0.8528
Upper notch	2.0971	1.2544	1.2120	0.2803	1.0214	1.1146	-1.6305	-1.0421	-1.2389	-0.6095
IQR	0.7433	0.7436	0.8102	0.6889	0.2507	0.3906	1.1315	0.6221	0.4582	0.5139
Q1	1.4969	0.7746	0.6165	-0.1154	0.8376	0.7354	-2.9063	-1.5782	-1.5733	-0.9883
Q3	2.2402	1.5182	1.4268	0.5735	1.0883	1.1259	-1.7748	-0.9560	-1.1151	-0.4744
#Outliers	1	0	1	0	2	2	0	2	0	0
#Sample	63	84	63	84	64	80	24	44	24	44

Figure 5. *Upper panel:* log([O ɪ]6300/Hα) versus log([O ɪɪ]3727 /[O ɪɪɪ]5007) diagram, with some structures – either LISs or Rims/Shells – that move away from the bulk of the data in their respective group lying in the transition zone marked with arrows (see the text). *Lower panel:* Same diagram, with the confidence ellipses of 1, 2 and 3σ.

two large grids of photoionization and shock models in the Mexican Million Models database (3MdB, Morisset et al. 2015; Alarie & Morisset 2019) allows us to explore the range of line ratios for both excitation mechanisms and for a wide range of physical parameters (see Appendix B for more details about the grid of models).

In Figure 6, we present a number of emission line DDs, including the common BPT and SMB diagrams, combining the predictions

from the grids of photoionization and shock models. Only the photoionization models that satisfy the criteria in Delgado-Inglada et al. (2014) with a sub-solar abundances set (log(O/H)=-3.66), a blackbody approximation for the energy distribution of the central source and constant density law are used. On the other hand, the grid of shock models is constrained by the following properties. i) Cut-off temperature ($T_{cut-off}$) and pre-shock temperature ($T_{pre-shock}$) both, <12500 K. ii) Shock-velocity between 10 and 100 kms^{-1} (slow shock models, Alarie & Morisset 2019) and between 100 and 350 kms^{-1} (fast-shock models, Allen et al. 2008; Morisset et al. 2015). iii) A sub-solar abundances set (namely, Allen2008_Dopita2005) for both subsets. iv) A pre-shock density between 10 and 100 cm^{-3} for the slow-shock models and 1 cm^{-3} for the fast-shock models, for comparability reasons. And v) a transverse magnetic field <10μG for both subsets of shock models.

An important overlap between the photoionization and shock models, especially for the low-ionization line ratios, is apparent. It is also evident that the common log(Hα/[S ɪɪ])<0.4 criterion for shock-excited supernova remnants (e.g., Leonidaki et al. 2013; Kopsacheili et al. 2020) does not adequately distinguish the two mechanisms. Although, it is possible to get such low Hα/[S ɪɪ] ratio from photoionization models with logU<-3.5 (see upper, right panel in Figure 6), resembling low- and high-velocity shock models.

Based on the BPT DDs, the low-velocity shock models (orange contours) cover a wide range of [O ɪɪɪ]/Hβ values from -5 to 0.5 (in logarithmic scale), but narrower ranges are covered by the [O ɪ]/Hα, [S ɪɪ]/Hα and [N ɪɪ]/Hα line ratios (Fig. 6). On the other hand, the complete (see caption of Fig. 6) fast-shock models yield, [O ɪɪɪ] λ5007/Hβ between -1 and 1. It should be noted that log([O ɪɪɪ] λ5007/Hβ)>0.5 is only produced by fast-shock models and photoionization models. Therefore, the [O ɪɪɪ] λ5007/Hβ ratio is a tracer of fast and slow shocks. Note that, shock models that produce log[O ɪɪɪ]/Hβ~1 and [O ɪ]/Hα~-2.0 are characterized by $T_{cut-off} \gtrsim 12000$ K (the higher the $T_{cut-off}$ the lower the [O ɪ]/Hα ratio; see Appendix B). The increase of the [O ɪ]/Hα and [S ɪɪ]/Hα line ratios in fast-shock models is followed by a decrease of the [O ɪɪɪ]/Hβ ratio, while the low-velocity shocks models do not show this dependency (see at the BPT diagrams).

The [O ɪɪ]/[O ɪɪɪ] versus [O ɪ]/Hα diagnostic diagram can also be used to determine the dominant excitation mechanisms of the nebulae. Fast shock (complete models) are restricted to a very narrow range of values (-0.5<log([O ɪɪ]/[O ɪɪɪ])<1), while the slow shock models have a minimum value of ~-2 and significantly higher values than fast shock models. The incomplete fast shock models can yield to lower [O ɪɪ]/[O ɪɪɪ] and [O ɪ]/Hα line ratios. On the other
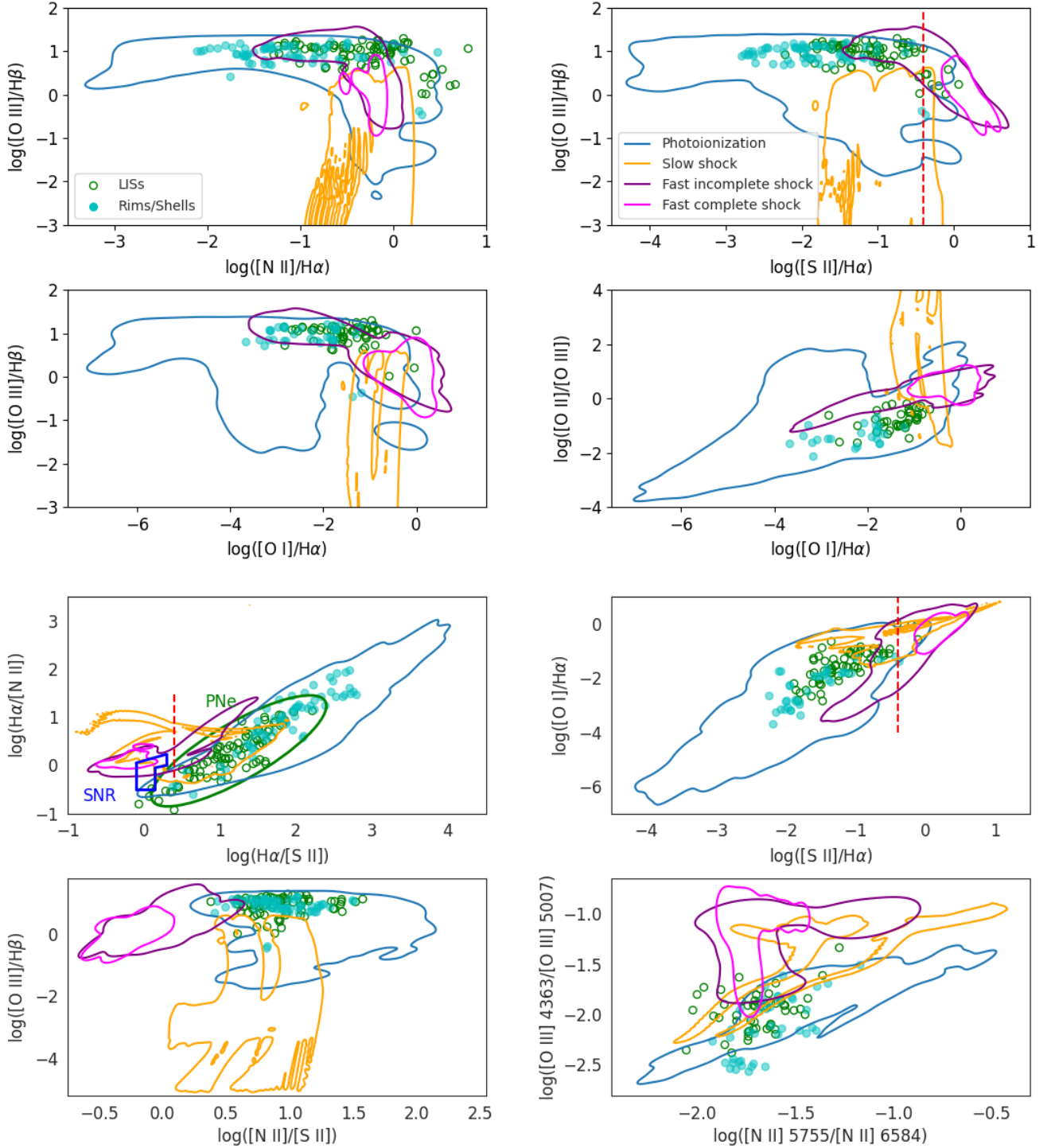
Figure 6. Emission-line diagnostic diagrams generated from grids of photoionization and shocks models available in the 3MBD. The photoionization models are presented with a blue contour, the low-velocity with an orange contour and the complete/incomplete high velocity shocks models with purple/magenta contours, respectively. The different contours cover the 98 percent of the total grids. Our sample of LISs and Rims/Shells are shown with unfilled green circles and filled cyan circles. The common log([S ɪɪ]/Hα)>-0.4 selection criterion for shock-excited supernova remnants (e.g. Leonidaki et al. 2013; Kopsacheili et al. 2020) is shown with a dashed-red line.

hand, most of the photoionization models display a linear increase of [O II]/[O III] as a function of the [O I]/Hα ratio, as we can observe in Figure 6. There are though models that break this relation, with 0<log([O II]/[O III])<2 and -4<log([O I]/Hα)<-2, and they are characterized by low-temperature central sources (<60000 K; see Appendix B).

The locus of PNe and supernova remnants (SNRs) in the SMB (Hα/[N II] 6548+6584 versus Hα/[S II] 6716+6731) diagnostic diagram are also displayed. The bulk of shock models do not totally coincide with the region of observed SNRs, and this is attributed to the chemical abundances of these models. The lower the abundance of N, lower the [N II] 6548+6584/Hα. The same result was also reported by Leonidaki et al. (2013) based on the spectroscopic observations of several SNRs in galaxies with different metallicities. The Hα/[S II] 6716+6731 ratio also follows the same relation with abundances. The lower the abundance of S, lower the [S II] 6716+6731/Hα ratio.

The [O I]/Hα versus [S II] 6716+6731/Hα diagram shows a small overlap between the predicted line ratios of the two mechanisms, being among the most crucial diagnostics for disentangling the shock-heated and photo-heated nebulae, as it has already been shown (e.g. Phillips & Guzman 1998; Leonidaki et al. 2013; Akras & Gonçalves 2016; Kopsacheili et al. 2020). Scrutinizing the models from 3MdB, we found that only photoionization models with logU<-3 are able to produce line ratios compatible to those of shock models. Therefore, this diagram can be a very helpful diagnostic tool. We argue that a selection criteria log([O I]/Hα)>-2 in conjunction with the common log([S II] 6716+6731/Hα)>-0.4 can provide shock-heated nebulae with high confidence and fewer contaminants.

The diagnostic diagram based on [O III]/Hβ versus [N II]/[S II] line ratios is also presented in Fig. 6. High-velocity shock models display a clear separation from the bulk of photoionization models, with [N II]/[S II]<0.4. On the contrary, the slow-velocity shock models overlap with photoionization models for 0.4<log([N II]/[S II])<0.9. Hence, the [N II]/[S II] line ratio can also be useful to constrain at least the shock velocity.

The last diagnostic diagram explored in this work involves the temperature sensitive line ratios, [O III] 4363/5007 and [N II] 5755/6584, and it provides a better separation between the shock-heated and photoionized nebular gases. An upper bound in log([O III] 4363/5007) is found for the photoionization mechanism of ~ -1.5, while there is no difference in log([N II] 5755/6584). The overlap between shock and photoionization models is minimal, and a selection criterion log([O III] 4363/5007)≥-1.5 can also be suitable for determining the excitation mechanism. Log([O III] 4363/5007) never takes values lower than -1.1 in shock models with transverse magnetic field <5μG. This agrees with the results from the bow-shock models of K 4-47 with log([O III] 4363/5007)~-1, significantly higher than the observed values -1.3 and -1.5 of the two knots (Gonçalves et al. 2004). The pre-shock magnetic field in these bow-shock models was considered negligible. Therefore, in case shocks take place in K 4-47 due to the highly moving knots, a magnetic field >5μG should be present. A few LISs are found to agree with low-velocity shock models characterized by log([N II] 5755/6584)≲-1.7 and log([O III] 4363/5007)≥-2.2, but the UV photoionization process cannot be ruled out.

According to the analysis above, we conclude that there is a significant overlap between the modelled predictions from the two mechanisms depending on the line ratio, and it is not feasible to disentangle the photo-heated and shock-heated gases based on individual line ratios, a combination of different line ratios is more efficient. The comparison of the observations with the models does not support the

scenario in which shock interactions is the dominant mechanism for the majority of the LISs.

5 DISCUSSION

In order to obtain more reliable and comprehensive conclusions regarding the LISs in PNe, a statistical analysis of their physicochemical properties and emission line ratios was carried out using the largest sample gathered so far. In the following, we discuss the different aspects addressed throughout the work, trying to emphasize, if present, the variations between the LISs, rims and shells of PNe.

5.1 Electron density

Considering a sample of 79 Rims/Shells and 98 LISs, the comparison between the two groups in Fig. 1 and Table 2 clearly shows that indeed LISs represent a statistically different sample than Rims/Shells in terms of electron density, as previously shown for several PNe individually. The median N_e[S II] of the LISs distribution (~1700 cm^{-3}) is approximately 0.6 lower than that of the PNe rims and shells (~2700 cm^{-3}). An additional way of emphasizing the discrepant electron densities of the two types of nebular components is shown in Fig. 7, top-left panel, which contrasts, per PN, the median N_e[S II] of Rims/Shells and LISs. This approach allows to reach exactly the same conclusions that LISs' electron densities are lower than those of rims and shells.

5.2 Electron temperature

Taking into account the electron temperature estimated from the [N II] diagnostic lines, we observed that there is no significant variation between the two groups (see Fig. 1). The median values of both distributions differ by ~0.2%, with overlapping notches. The distribution of the [N II] 5755/6584 line ratio for the two groups displays a similar range of values from -2 to -1 (in logarithmic scale, see Figure 6). The two groups also have the same median values (not shown here; -1.70 and -1.71 for the Rims/Shells and LISs, respectively, and comparable lower/upper notches of -1.741/-1.676 for LISs and -1.757/-1.658 for Rims/Shells). Since in the higher ionization structures the N^{++} recombination line could contribute to the [N II] 5755 Å auroral line emission, the identity between the two groups suggests that the N^{++} recombination is negligible.

Regarding T_e[O III], we note that the median value of the Rims/Shells group (T_e ~10200K) is ~0.88 times lower than that of the LISs (T_e ~11600K), whereas the notches of both distributions do not overlap. Therefore, it can be argued that the two groups are statistically different, as far as T_e[O III] is concerned. A possible interpretation of the different distributions between LISs and Rims/Shells subsets [O III] temperature could be that the higher electron temperatures in some particular LISs are associated with external heating mechanisms, such as shocks or photoelectric heating by dust grains. For gases with T_e>8000 K, heating by dust grains is insignificant due to the electron-grains collisions (Draine 1978), except if large molecules like PAHs are also present (Lepp & Dalgarno 1988). The molecular hydrogen emission found in LISs (Akras et al. 2017, 2020c) points out the presence of an amount of dust which prevents the dissociation of H_2 molecules, while PAHs may also be present and responsible for the formation of H_2 (e.g. Boschman et al. 2015).

The veracity of the above trend for temperatures, can be more stringently tested by the analysis, per nebula, of the median T_e ([O III] and [N II]) of the two types of components, as shown in Table 6 and

Fig. 7. From the top-right panel it can be seen that both differences of electron temperatures estimated through the [N II] and [O III] diagnostics exhibit a ±2000 K dispersion centred around zero. This reflects the uncertainties of the estimations, therefore the average ~1400 K higher T_e[O III] of LISs quoted above is within the scatter and cannot be taken as significant. The median values of the two electron temperatures, as in Table 6, are also plotted for Rims/Shells versus LISs in the bottom panels of Fig. 7, which again clearly show that taking the dispersion into account, neither T_e[O III] nor T_e[N II] show significant discrepancies between LISs and Rims/Shells.

5.3 Abundances

We did not find any statistically significant difference in the chemical abundances of He, O, N, Ne, Ar, S and Cl between the LISs and the high-ionization rims and shells (see Fig. 2 and Table 3).

The linear abundances' ratio correlations analyzed also do not show significant differences (slopes and intercepts) independently of the LISs' inclusion in the correlations (see Table 4). Slope and intercepts are similar, taking into account their uncertainties, with and without the LISs. The goodness-of-fit, on the other hand, slightly decreases when the LISs are considered. LISs add scatter in the correlations, because of their usually lower S/N ratio in comparison with rims and shells. The correlation found between log(N/H) versus log(N/O) is found to agree, within error, with previous studies (e.g. García-Rojas et al. 2013; Akras & Gonçalves 2016).

As in the cases of T_e and N_e, we also examine the veracity of the chemical abundances trends. Figure 8 shows the distributions of the median values, per chemical element and nebula, for LISs and Rims/Shells. It can be seen that the majority of the structures lie near the identity line, although with dispersion. It is important to note that the samples used are small. Nonetheless, it is verified that the abundances between the two groups do not differ significantly, as previously established (see Fig 2).

5.4 Excitation mechanism

SMB's and BPT's emission-line ratio diagrams were used in an attempt to found any significant difference between the excitation processes dominating Rims/Shells and LISs. From SMB, it is observed that most LISs are in the PNe region, with higher [N II]/Hα and [S II]/Hα ratios compared to the Rims/Shells. From their violinplots distributions and corresponding statistical parameters, we verified that there is no overlap between the two groups. Concerning the BPT, we found that LISs and Rims/Shells exhibit different median [O III] λ5007/Hβ face values, with the latter slightly lower, while their notches do overlap. As for the [O III] λ4363/Hβ ratio, the statistics shows similar medians and clear overlapping. Motivated by the large [O III] λ4363/Hβ ratios found in LISs, we also explore the high-ionization line ratio He II λ4686/Hβ. Despite, LISs have lower median values than rims and shells, there is a number of LISs with He II λ4686/Hβ between 0.7-1 (e.g. Wray17-1, K 1-2, Hu1-2, Necklace among others). This particular subgroup of PNe display complex morphologies with highly-collimated or jets or jet-like structures. Furthermore, the host nebulae of this subgroup of LISs also exhibit high He II λ4686/Hβ.

An analysis of the two groups based on the [O II]λ3727/λ5007 versus [O I]λ6300/Hα diagram was also performed, and a clear separation between the Rims/Shells and LISs is observed. LISs occupy the top-right corner, with high values of [O II] and [O I], while the Rims/Shells are located in the bottom-left corner. This result is

also verified with the split violinplots, where their medians differ at a 95 percent confidence level (see Table 5). Combining emission lines of the same element (oxygen), from three different ionization states, we highlight the different ionization state of LISs and host nebulae, avoiding the effect of the chemical abundance of the combination of different elements, as in the previous diagrams.

5.5 Model predictions

The intriguing characteristics of low-ionization structures relative to their host PNe has been calling astronomers' attention for several years regarding their origin and the dominant excitation mechanism (photoionization and shock-heating processes). Their usually stronger low-ionization lines relative to Hα (e.g., [N II] 6548+6584/Hα, [S II] 6716+6731/Hα, [O I] 6300/Hα) have been attributed either shocks (e.g. Hartigan et al. 1994; Dopita 1997; Gonçalves et al. 2004; Akras & Gonçalves 2016) or UV photoionization process (e.g. Hajian et al. 1997; Gonçalves et al. 2003; Ali & Dopita 2017).

The recent discoveries of molecular hydrogen (H$_2$) associated with LISs (Fang et al. 2015; Akras et al. 2017; Fang et al. 2018; Akras et al. 2020c) have entailed the presence of highly dense gas ($>10^{4-5}$ cm^{-3}) to shelf-shield the molecular component and prevent its dissociation. Such high-density structures are able to produce strong low-ionization lines similar to photo-dissociation regions (PDRs) or low-ionization nebulae (low logU).

To further investigate the dominant mechanisms in LISs, we compared the observations with the predictions from photoionization and shock models. The regions occupied by LISs, Rims/Shells and the distribution of fast/slow shock models and photoionization models are presented in eight emission line DDs in Fig. 6. At first look, we find a very good match between the observations and the regime of photoionization models (blue contour) in all DDs, but shock can not be easily ruled out as several line ratios can also be reproduced by fast- or slow-shock models.

It should be noted that Rims/Shells and LISs show a different slope in the [O II]/[O III] versus [O I]/Hα DD (see Fig 5), indicating a different ionization state in LISs relative to their host PNe, such as a mini-PDR around a dense molecular core.

Concerning the widely used SMB – Hα/[N II] 6548+6584 versus Hα/[S II] 6716+6731 – diagnostic diagram (Sabbadin et al. 1977), we demonstrate that LISs lie in the bottom-left corner of the PNe locus, close to the locus of observed SNRs. Besides low-ionization models (logU<-3), only shock with velocities <100 km s^{-3} are able to produce Hα/[N II] and Hα/[S II] 6716+6731 line ratios similar to LISs, but fail to reproduce other lines.

LISs are found to exhibit a systematic higher T_e[O III] than Rims/Shells but comparable T_e[N II] (see Fig. 1 and Table 2). A statistical analysis on the temperature sensitive diagnostic line ratios has also been performed. LISs are characterized by a median log([O III] λ4363/λ5007)=-1.9505 higher than the median of rims and shells (-2.0303). This deviation is statistically significant if we take into account the lower/upper notches (LISs: -1.9989/-1.9021, Rims/Shells:-2.1236/-1.937), which demonstrate the 95 percent of the confidence-interval (CI) for the median values.

The distribution of the LISs and Rims/Shells subsets in the [O III] λ4363/λ5007 versus [N II] λ5755/λ6584 DD is presented in Fig. 6. Most of the data points lie well within the regime of photoionization models. There is, though, a distinct small group of LISs which display an enhanced [O III] λ4363/λ5007 ratio relative to the predicted ratio from photoionization models, lying in an area where only low-velocity shock models are found. This particular group of
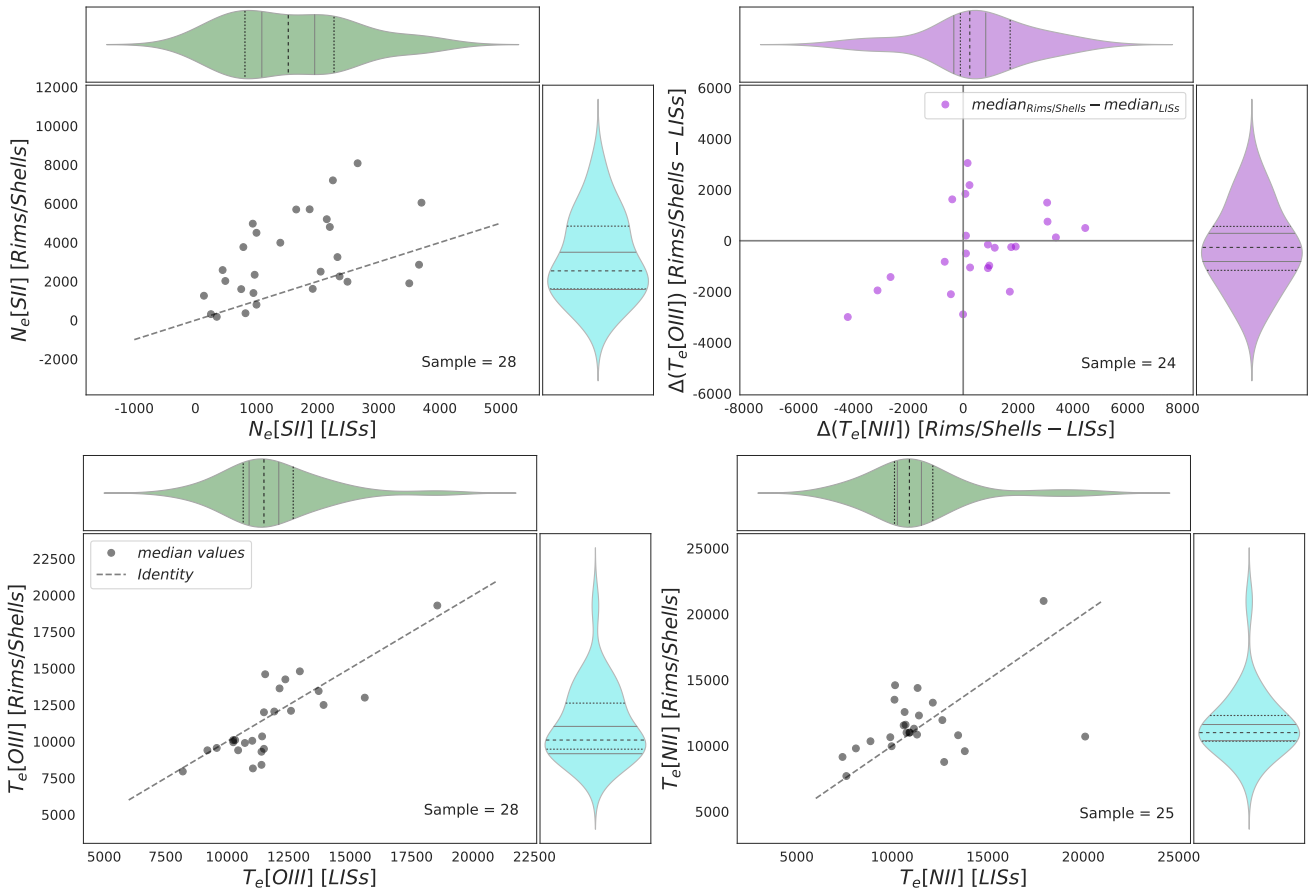
Figure 7. Comparison of median T$_e$ and N$_e$ between Rims/Shells and LISs, for each nebula in the sample, as in Table 6. The dashed-lines represent the identity function.

LISs includes the following PNe: Hen 2-186 (1 LIS), NGC 3918 (2 LISs), NGC 6543 (1 LIS), K 1-2 (3 LISs), NGC 6572 (1) Hen 1-1 (1 Rim/Shell), KjPn8 (1 LIS), and NGC 7009 (1 LIS). We should also mention that log([O III] $\lambda4363/\lambda5007$)>-1.5 seems to be a good indicator of shock-heated gas. Leung et al. (2021) also came to a similar conclusion based on AGN and shock models. More specifically, AGN models cannot reach log([O III] $\lambda4363/\lambda5007$) higher than -1.5 for any log(U) value, while shock models yield values between -2 and -1, in agreement with our results (see figures 12 and 13 in Leung et al. 2021). It is worth mentioning that the criterion log([O III] $\lambda4363/\lambda5007$)>-1.5 is valid only for environments with density $\leq7\times10^5$ cm^{-3} (critical density of the [O III] 5007Å line). In the case of a denser gas, the [O III] 5007Å line will be collisionally de-excited and will result in a high [O III] $\lambda4363/\lambda5007$ ratio resembling shock-heated gas.

6 CONCLUSIONS

The main conclusions extracted from the physical, chemical and excitation properties of the largest sample of LISs, rims and shells of PNe analyzed so far are listed below.

• LISs are statistically different from Rims/Shells in terms of N$_e$[S II]. The former exhibit ~2/3 lower electron density (~1700 cm^{-3}) than the latter (~2700 cm^{-3}) components.
• Though LISs have median T$_e$[O III] comparable with those of the Rims/Shells, respectively ~11600K and ~10200 K (both with

large dispersion), the distribution [O III] temperatures also has a well-marked bimodality, not easily explained. The [N II] electron temperatures show no difference between the two types of nebular components, LISs and Rims/Shells, with a median value of ~10800 K.

• No statistical difference in the chemical composition is found between LISs and Rims/Shells, based on the analysis of helium, nitrogen, oxygen, neon, argon, chlorine and sulphur.

• Shock models with low-velocity shocks, as well as photoionization modelling of PNe with low ionization parameter are both able to produce the line ratios found in LISs.

• The [N II]/[S II]≤0.25 ratio is found to distinguish fast-shock (>100 km s^{-1}) models from photoionization and slow-shock models.

• The diagnostic diagram of the temperature dependent ratios shows that log([O III] 4363/5007)>-1.5 is a good tracer of shock-heated gas, for electron densities <7×10^5 cm^{-3}.

• The vast majority of LISs and Rims/Shells have line ratios in agreement with the predictions of the photoionization models, yet there are a few LISs for which shocks could be present.

• Individual line ratios are not adequate to distinguish photoheated and shock-heated gas, a combination of them provides a more robust separation.

Table 6. Median T$_e$ and N$_e$ for Rims/Shells and LISs, per nebula.

Name	N$_e$[S II]		T$_e$[N II]		T$_e$[O III]		References
	m$_{Rims/Shells}$	m$_{LISs}$	m$_{Rims/Shells}$	m$_{LISs}$	m$_{Rims/Shells}$	m$_{LISs}$	
NGC 6543	4800	2200	9150	7400	7950	8200	Balick et al. (1994)
NGC 6826	800	1000	7700	7600	9400	9200	Balick et al. (1994)
NGC 7009	4500	1000	9800	8100	9500	11500	Balick et al. (1994)
Hb 4	3770	790	10650	9900	8550	-	Hajian et al. (1997)
IC 4634	8080	2660	11000	10750	9400	10450	Hajian et al. (1997)
NGC 6369	2020	490	10850	11300	9300	11400	Hajian et al. (1997)
NGC 7354	2340	970	11100	-	9950	10250	Hajian et al. (1997)
M 2-48	1260	140	10700	20100	10850	-	López-Martín et al. (2002)
NGC 7009	5700	1650	11600	10700	10100	10250	Gonçalves et al. (2003)
K 4-47	1900	3500	21000	17930	19300	18550	Gonçalves et al. (2004)
NGC 7662	2500	2050	14600	10150	12000	11500	Perinotto et al. (2004)
IC 4634	5200	2150	11550	10600	10050	11030	Guerrero et al. (2008)
He 1-1	1600	750	10800	13450	12500	13930	Gonçalves et al. (2009)
IC 2149	6050	3700	12300	11400	10350	11430	Gonçalves et al. (2009)
KjPn 8	-	600	-	9030	-	10330	Gonçalves et al. (2009)
NGC 7662	3250	2330	13280	12130	13450	13730	Gonçalves et al. (2009)
NGC 7354	1980	2490	14390	11330	13630	12140	Contreras et al. (2010)
Necklace	360	820	11000	10920	14800	12960	Corradi et al. (2011)
ETHOS1	-	-	-	-	-	-	Miszalski et al. (2011)
NGC 3242	2860	3660	13500	10120	12050	11920	Monteiro et al. (2013)
Hu 1-2	-	-	-	-	-	-	Fang et al. (2015)
IC 4846	7200	2250	11950	12630	9900	10730	Akras & Gonçalves (2016)
Wray 17-1	180	350	-	12250	14250	12370	Akras & Gonçalves (2016)
K 1-2	-	610	-	9120	-	14250	Akras & Gonçalves (2016)
NGC 6891	1400	950	9628	-	9560	9580	Akras & Gonçalves (2016)
NGC 6572	20840	10120	12570	10650	10100	10330	Akras & Gonçalves (2016)
M 2-42	2580	450	10340	8860	-	-	Danehkar et al. (2016)
NGC 5307	-	2950	-	13090	-	12330	Ali & Dopita (2017)
IC 2553	-	2400	-	10790	-	10930	Ali & Dopita (2017)
PB 6	-	1510	-	11150	-	13750	Ali & Dopita (2017)
NGC 3132	-	100	-	13600	-	-	Monreal-Ibero & Walsh (2020)
IRAS	1620	1920	8770	12720	-	-	Miranda et al. (2021)
Hen 2-186	3990	1390	11300	11140	14600	11550	Mari et al. (2023)
Hen 2-429	5710	3760	9390	-	9790	-	Mari et al. (2023)
IC 4593	2260	2360	9590	13800	8410	11400	Mari et al. (2023)
NGC 3918	5710	1870	11000	10900	12100	12600	Mari et al. (2023)
NGC 6543	4970	940	9970	9970	8160	11050	Mari et al. (2023)
NGC 6905	310	260	-	-	13000	15600	Mari et al. (2023)

DATA AVAILABILITY

The two grids of photoionization and shock models underlying this article are available in the Mexican Million Models database.

REFERENCES

Akras S., Gonçalves D. R., 2016, MNRAS, 455, 930
Akras S., Gonçalves D. R., Ramos-Larios G., 2017, MNRAS, 465, 1289
Akras S., Gonçalves D. R., Ramos-Larios G., Aleman I., 2020a, Galaxies, 8, 30
Akras S., Monteiro H., Aleman I., Farias M. A. F., May D., Pereira C. B., 2020b, MNRAS, 493, 2238
Akras S., Gonçalves D. R., Ramos-Larios G., Aleman I., 2020c, MNRAS, 493, 3800
Akras S., et al., 2022, MNRAS, 512, 2202
Alarie A., Drissen L., 2019, MNRAS, 489, 3042
Alarie A., Morisset C., 2019, Rev. Mex. Astron. Astrofis., 55, 377
Ali A., Dopita M. A., 2017, Publ. Astron. Soc. Australia, 34, e036
Allen M. G., Groves B. A., Dopita M. A., Sutherland R. S., Kewley L. J., 2008, ApJS, 178, 20
Baldwin J. A., Phillips M. M., Terlevich R., 1981, PASP, 93, 5
Balick B., 1987, AJ, 94, 671
Balick B., Frank A., 2002, ARA&A, 40, 439
Balick B., Rugers M., Terzian Y., Chengalur J. N., 1993, ApJ, 411, 778
Balick B., Perinotto M., Maccioni A., Terzian Y., Hajian A., 1994, ApJ, 424, 800
Balick B., Alexander J., Hajian A. R., Terzian Y., Perinotto M., Patriarchi P., 1998, AJ, 116, 360
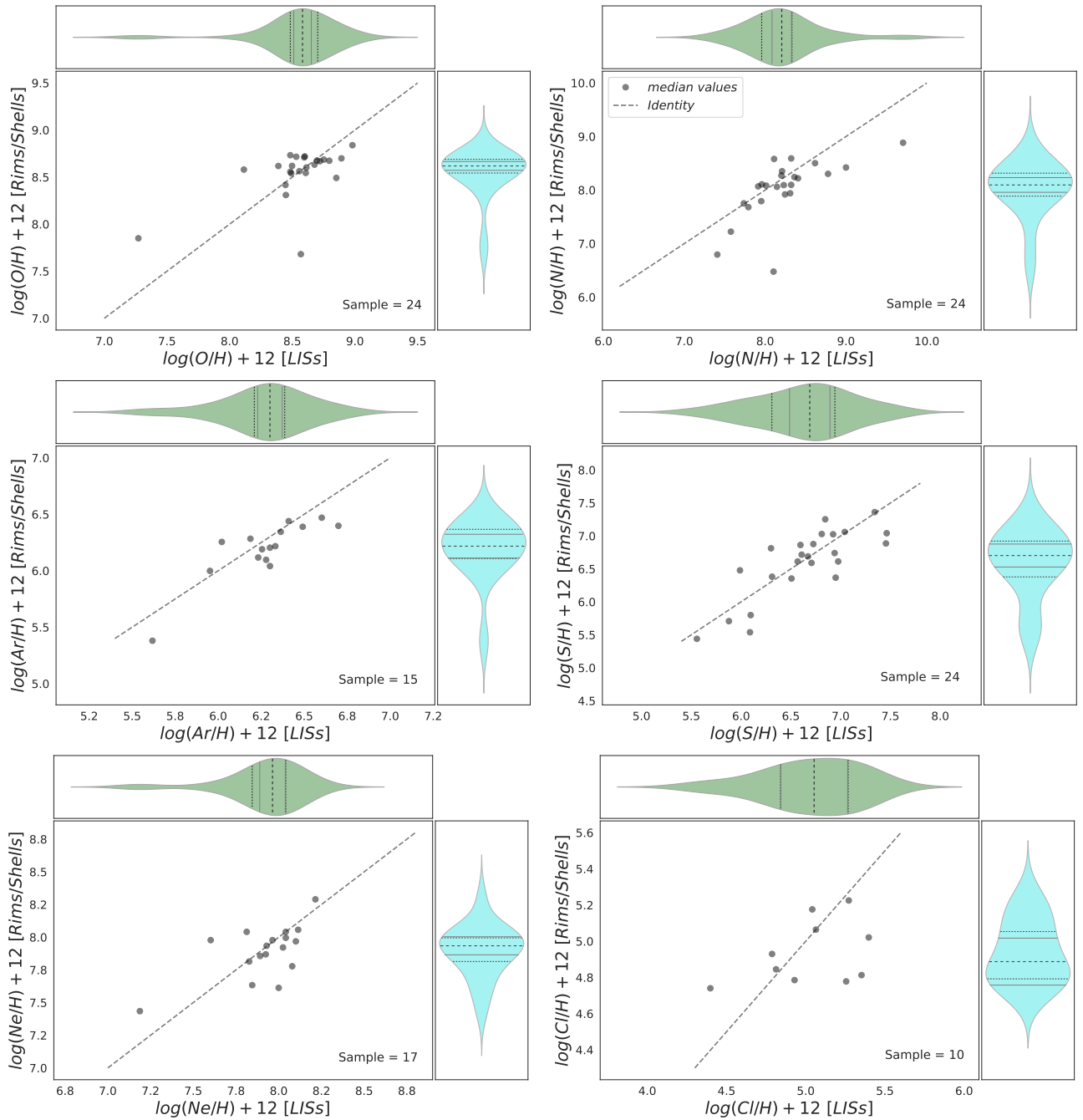Balick B., Frank A., Liu B., 2020, ApJ, 889, 13
Bohigas J., 2008, ApJ, 674, 954

Figure 8. Same as Fig. 7 for total abundances.

Boschman L., Cazaux S., Spaans M., Hoekstra R., Schlathölter T., 2015, A&A, 579, A72

Cavichia O., Costa R. D. D., Maciel W. J., 2010, Rev. Mex. Astron. Astrofis., 46, 159

Cavichia O., Costa R. D. D., Maciel W. J., Mollá M., 2017, MNRAS, 468, 272

Chambers J. M., Cleveland W. S., Kleiner B., Tukey P. A., 2017, Graphical Methods for Data Analysis. 1st Edition, doi:10.1201/9781351072304

Contreras M. E., Vázquez R., Miranda L. F., Olguín L., Zavala S., Ayala S., 2010, AJ, 139, 1426

Corradi R. L. M., Manso R., Mampaso A., Schwarz H. E., 1996, A&A, 313, 913

Corradi R. L. M., et al., 2011, MNRAS, 410, 1349

Danehkar A., Parker Q. A., Steffen W., 2016, AJ, 151, 38

De Marco O., et al., 2022, Nature Astronomy, 6, 1421

Delgado-Inglada G., Morisset C., Stasińska G., 2014, MNRAS, 440, 536

Dopita M. A., 1997, ApJ, 485, L41

Dopita M. A., Sutherland R. S., 1995, ApJ, 455, 468

Draine B. T., 1978, ApJS, 36, 595

Exter K. M., Pollacco D. L., Bell S. A., 2003, MNRAS, 341, 1349

Fang X., Guerrero M. A., Miranda L. F., Riera A., Velázquez P. F., Raga A. C., 2015, MNRAS, 452, 2445

Fang X., Zhang Y., Kwok S., Hsia C.-H., Chau W., Ramos-Larios G., Guerrero M. A., 2018, ApJ, 859, 92

Ferland G. J., et al., 2017, Rev. Mex. Astron. Astrofis., 53, 385

Frew D. J., Parker Q. A., 2010, Publ. Astron. Soc. Australia, 27, 129

García-Rojas J., Peña M., Morisset C., Delgado-Inglada G., Mesa-Delgado A., Ruiz M. T., 2013, A&A, 558, A122

Gonçalves D. R., Corradi R. L. M., Mampaso A., 2001, ApJ, 547, 302

Gonçalves D. R., Corradi R. L. M., Mampaso A., Perinotto M., 2003, ApJ, 597, 975

Gonçalves D. R., Mampaso A., Corradi R. L. M., Perinotto M., Riera A., López-Martín L., 2004, MNRAS, 355, 37

Gonçalves D. R., Mampaso A., Corradi R. L. M., Quireza C., 2009, MNRAS, 398, 2166

Górny S. K., Schwarz H. E., Corradi R. L. M., Van Winckel H., 1999, A&AS, 136, 145

Guerrero M. A., et al., 2008, ApJ, 683, 272

Guerrero M. A., Suzett Rechy-García J., Ortiz R., 2020, ApJ, 890, 50

Hajian A. R., Balick B., Terzian Y., Perinotto M., 1997, ApJ, 487, 304

Hartigan P., Morse J. A., Raymond J., 1994, ApJ, 436, 125

Henry R. B. C., 1990, ApJ, 356, 229

Hintze J. L., Nelson R. D., 1998, The American Statistician, 52, 181

Hora J. L., Latter W. B., Allen L. E., Marengo M., Deutsch L. K., Pipher J. L., 2004, ApJS, 154, 296

Kopsacheili M., Zezas A., Leonidaki I., 2020, MNRAS, 491, 889

Krzywinski M., Altman N., 2014, Nature Methods, 11, 119

Leonidaki I., Boumis P., Zezas A., 2013, MNRAS, 429, 189

Lepp S., Dalgarno A., 1988, ApJ, 335, 769

Leung G. C. K., Coil A. L., Rupke D. S. N., Perrotta S., 2021, ApJ, 914, 17

López-Martín L., et al., 2002, A&A, 388, 652

Lumsden S. L., Puxley P. J., Hoare M. G., 2001, MNRAS, 328, 419

Maciel W. J., Costa R. D. D., Cavichia O., 2017, Rev. Mex. Astron. Astrofis., 53, 151

Manchado A., Guerrero M. A., Stanghellini L., Serra-Ricart M., 1996, The IAC morphological catalog of northern Galactic planetary nebulae. -

Mari M. B., Gonçalves D. R., Akras S., 2023, MNRAS, 518, 3908

Mata H., et al., 2016, MNRAS, 459, 841

Matsuura M., et al., 2009, ApJ, 700, 1067

Miranda L. F., et al., 2021, arXiv e-prints, p. arXiv:2105.05186

Miszalski B., Corradi R. L. M., Boffin H. M. J., Jones D., Sabin L., Santander-García M., Rodríguez-Gil P., Rubio-Díez M. M., 2011, MNRAS, 413, 1264

Monreal-Ibero A., Walsh J. R., 2020, A&A, 634, A47

Monteiro H., Gonçalves D. R., Leal-Ferreira M. L., Corradi R. L. M., 2013, A&A, 560, A102

Morisset C., Delgado-Inglada G., Flores-Fajardo N., 2015, Rev. Mex. Astron. Astrofis., 51, 103

Perinotto M., Patriarchi P., Balick B., Corradi R. L. M., 2004, A&A, 422, 963

Phillips J. P., Guzman V., 1998, A&AS, 130, 465

Raga A. C., Riera A., Mellema G., Esquivel A., Velázquez P. F., 2008, A&A, 489, 1141

Rauch T., 2003, A&A, 403, 709

Riesgo H., López J. A., 2006, Rev. Mex. Astron. Astrofis., 42, 47

Sabbadin F., Minello S., Bianchini A., 1977, A&A, 60, 147

Sabin L., et al., 2013, MNRAS, 431, 279

Schwarz H. E., Corradi R. L. M., Melnick J., 1992, A&AS, 96, 23

Steffen W., López J. A., Lim A., 2001, ApJ, 556, 823

Sutherland R. S., Dopita M. A., 2017, ApJS, 229, 34

Sutherland R., Dopita M., Binette L., Groves B., 2018, MAPPINGS V: Astrophysical plasma modeling code (ascl:1807.005)

Tukey J. W., 1977, Exploratory data analysis. -

APPENDIX A: DATA VISUALIZATION

A representative – and classical – way to explore large datasets is through the use of histograms in order to determine the distribution of each feature under investigation. Alternatively, the use of diagrams such as *boxplots* (Tukey 1977) provides a better visualization for the quantities such as the quartiles, the median, the interquartile range (IQR) and also the outliers. The definition of these quantities is given below.
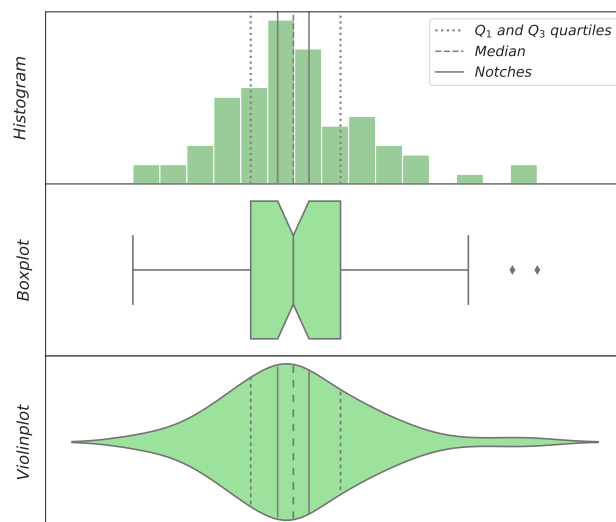

Figure A1. Distribution of a data sample for three different visualization plots: histogram, boxplot and violinplot. Q_1 and Q_3 quartiles represent the location of the 25th and 75th percentiles, respectively, and they are illustrated by vertical dash-dotted lines. The median values represent the 50th percentile, which is also the mid-point of the distribution, and it is shown by a vertical dashed line. The notches show the most likely values expected for the median, and they are represented by vertical solid lines. In the case of the boxplot, the actual structure of the boxes coincide with the aforementioned parameters. The violinplot also demonstrates the density distribution of a sample, where wider (narrower) regions represent a higher (lower) probability that members of the population adopt the given value.

- *Quartiles* specify the location of the 25th (Q1) and 75th (Q3) percentiles. The 25th percentile corresponds to the 25 percent of the values that are less than or equal to this value. A similar definition for the 75th percentile;

- *Median* represents not only the mid-point of the distribution but also the 50th (Q2) percentile;

- *Interquartile range (IQR)* is the distance/range between the third and first quartiles;

- The minimum *(min)* and maximum *(max)* value of the sample, excluding the outliers, which are determined for the distance between the first and third quartiles and 1.5 times the IQR[2];

- *Notches* Another very important parameter for a statistical approach is the *notches* (Chambers et al. 2017). The *notches* are related with the median, IQR and the number of observations/population (*n*) of each subset, and they are used to demonstrate the 95 percent of confidence interval (CI) for the median value: $m \pm 1.58 \times IQR/\sqrt{n}$. When the notches of two samples do not show an overlap, the medians of each of the distributions are considered significantly different (Krzywinski & Altman 2014). A possible overlap does not necessarily rule out the possibility that the two samples are different.

A second –and more integrated– visualization approach is through the use of *violinplots*, which combine a boxplot and kernel density estimation together in one diagram (Hintze & Nelson 1998). This representation of a data sample provides information about the shape of the distribution, such as their peaks and their positions, or even

---

[2] This is related to a characteristic of the Normal Distribution, the 1.5 in minimum and maximum value ends up being approximately $\pm 2.7\sigma$ (being σ the standard deviation) from the mean, which corresponds to a 99.3 percent of the data for a normal distribution. Then, any data point lower than (or greater than) the min (max) is considered as an outlier.

unveil the presence of clustering in the data (e.g. a bimodal distribution). Moreover, having the density distribution in the violinplots, it can be seen that the wider the section (the size of the violin in the y-axis of Figure A1, bottom panel) the higher that probability to get the corresponding value, whereas a narrower section represent a lower probability. Figure A1 illustrates these parameters on a violinplot, together with a boxplot and histogram, for comparison purposes.

APPENDIX B: 3MDB DATABASE

The grid of photoionization models in the 3MdB was constructed using CLOUDY v17.01 (Ferland et al. 2017) and covers a wide range of physical parameters: T_{eff} and L (or equivalently log(U)), chemical abundances, density and size (see Delgado-Inglada et al. 2014). The entire grid consists of 724,386 models, but only 116,121 of them are used that satisfy the criteria (flag com6=1) in Delgado-Inglada et al. (2014).

The stellar parameters of effective temperature (T_{eff}) and luminosity (L) of PNe central stars are crucial as they define the energy distribution of the ionizing photons responsible for the ionization and excitation of atomic gas. Hence, it is worth to explore the emission line ratios as functions of stellar T_{eff} and L. The grid of photoionization models in the 3MdB covers a range T_{eff} from 25 up to 300 kK for a black-body approximation, and from 50 to 180 kK using the atmosphere stellar models from Rauch (Rauch 2003), $2\times10^2 < L < 1.78\times10^4$ L⊙ and a wide range of density from 30 up to 3×10^5 cm^{-3}. No noticeable differences in the line ratios between the blackbody and atmosphere stellar models is found.

Photoionization models' entanglement with T_{eff} and L compels us to explore the more general value of the ionization parameter (logU) which encompass both stellar parameters, and it is more suitable and widely used. It is defined as the ratio of ionizing photon density to gas density multiplied by speed of light at a distance r from the central source (U(r)=Q/$4\pi r^2 n_H c$), where Q is the rate of ionizing photons and directly related with the stellar parameters, n_H the hydrogen density and c is the speed of light. This dimensionless parameter can easily distinguish regions that are UV-dominated or not, and it varies from -1 to -5.

Finally, four metallicities/abundances sets are available in the 3MdB: log(O/H)=-3.66, -3.36, -3.06 and -2.76 (see also Delgado-Inglada et al. 2014).

The shock models were generated using the code MAPPINGS V, version 5.1.13 (Sutherland & Dopita 2017; Sutherland et al. 2018). The total number of available shock models in the 3MdB is 199,750 and a wide range of physical parameters is covered such as the shock velocity, the pre-shock and cut-off temperatures, the ionization state of the pre-shocked gas, the pre-shock density and metallicity, and the pre-shock transverse magnetic field. For more details, we refer the reader to (Dopita & Sutherland 1995; Dopita 1997; Allen et al. 2008).

Five different metallicities/abundances sets (LMC, SMC, solar, twice-solar and one namely Allen2008_Dopita2005) were used for the total grid of high velocity shock models and only one abundance set (namely 3MdB-PNe2014-solar) for the low velocity shock models.

The pre-shock ($T_{pre-shock}$) and cut-off temperatures ($T_{cut-off}$) are among the most important parameters in shock models. At this point, it is noteworthy to define the complete and incomplete or truncated shock models. Complete shock models are like those from Allen et al. (2008) and they are defined as the shock models for which $T_{cut-off}$ =1000 K. Any change in $T_{cut-off}$ results in different spatial

extent of the post-shock regions and consequently to the integrated emission and line ratios.

$T_{cut-off}$ is the equivalent of T_e stopping criterion (4000 K) in the CLOUDY photoionization models (Ferland et al. 2017; Bohigas 2008). Both define the temperature of the gas at a certain distance behind the shock (or from the central star) at which the model must stop, as not significant emission is considered to emanate from these regions since the gas has cooled down and totally recombined. For the incomplete/truncated shock models in the 3MdB, $T_{cut-off}$ varies from 1000 up to 20000 K, and it has a significant impact on the resultant emission line spectra (e.g. Alarie & Morisset 2019; Alarie & Drissen 2019).

The temperature of the pre-shocked gas ($T_{pre-shock}$) has also an important effect on the predictions of shock models. In particular, shocks with velocities higher than 100 km s^{-1} can significantly alter the physical conditions and ionization structure of the pre-shocked gas, resulting in a wide range of shock spectra. On the other hand, shocks with velocities <75 km s^{-1} do not have any significant influence on the pre-shocked gas. Therefore, the grid of low shock velocity models has been built considering a priori different ionization fractions for the pre-shocked gas.

In Figure B1, we displays the dependence of various emission line ratios as functions of $T_{pre-shock}$, $T_{cut-off}$ and shock velocity for the high velocity incomplete grid of models (namely Allen2008_cut). Shock velocity is constrained to <500 km s^{-1} (and $T_{pre-shock}$ <15000 K) and the pre-shock transverse magnetic field <0.5 μG. The size of the symbols represent the velocity of the shock.

The [O I]/Hα, [N II]/Hα and [S II]/Hα line ratios decrease for higher $T_{cut-off}$, while [O III]/Hβ increases. Moreover, it should be pointed out that [O I]/Hα, [N II]/Hα and [S II]/Hα increase (or decrease) for higher shock velocity depending on the $T_{cut-off}$ parameter. For $T_{cut-off}$ >10000 K, the ratios decrease while for $T_{cut-off}$ <10000 K the ratios increase. As for [O III]/Hβ, it also increases as function of shock velocity but only in shock models with $T_{cut-off}$ <10000 K. For higher $T_{cut-off}$ <, the [O III]/Hβ ratio seems to be independent.

The [N II] 5755/6584 and [O III] 4363/5007 ratios are also presented in Figure B1. The former shows no correlation with $T_{pre-shock}$ or shock velocity but it become higher for increasing $T_{cut-off}$. The latter takes values in a very narrow range from -0.98 to -1.03 being nearly unaffected by the $T_{pre-shock}$ and $T_{cut-off}$ parameters.

Pre-shock density is also a crucial parameter in shock models. The grid of low velocity models (Alarie & Morisset 2019) was built considering four pre-shock densities: 10, 100, 1000 and 10000 cm^{-3}, whereas the grid of high velocity shock models (complete and incomplete; Allen et al. 2008) is constructed for only one pre-shock density (1 cm^{-3}). Only, the pre-shock density in the shock models with solar metallicity ranges from 0.01 up to 1000 cm^{-3}.

Last but not least, the pre-shock transverse magnetic field also has an important impact on the spectra and emission line ratios. It is found that the affect of pre-shock transverse magnetic field on the emission lines is more complicated. For the models with $T_{pre-shock}$ ≤13000 K and any value for $T_{cut-off}$, all the aforementioned ratios – [O I]/Hα, [N II]/Hα, [S II]/Hα, [O III]/Hβ, [N II] 5755/6584 and [O III] 4363/5007 – appear unaffected by the magnetic field. For the models with $T_{pre-shock}$ ≥13000 K and $T_{cut-off}$ ≥13000 K, the [O I]/Hα, [N II]/Hα and [S II]/Hα line ratios decrease for higher magnetic field while the [O III]/Hβ, [N II] 5755/6584 and [O III] 4363/5007 ratios are almost invariable. For the cases of $T_{pre-shock}$ ≥13000 K and $T_{cut-off}$ ≤13000 K, [O I]/Hα, [O III]/Hβ and [N II] 5755/6584 do not show significant changes, [N II]/Hα increases and [S II]/Hα and [O III] 4363/5007
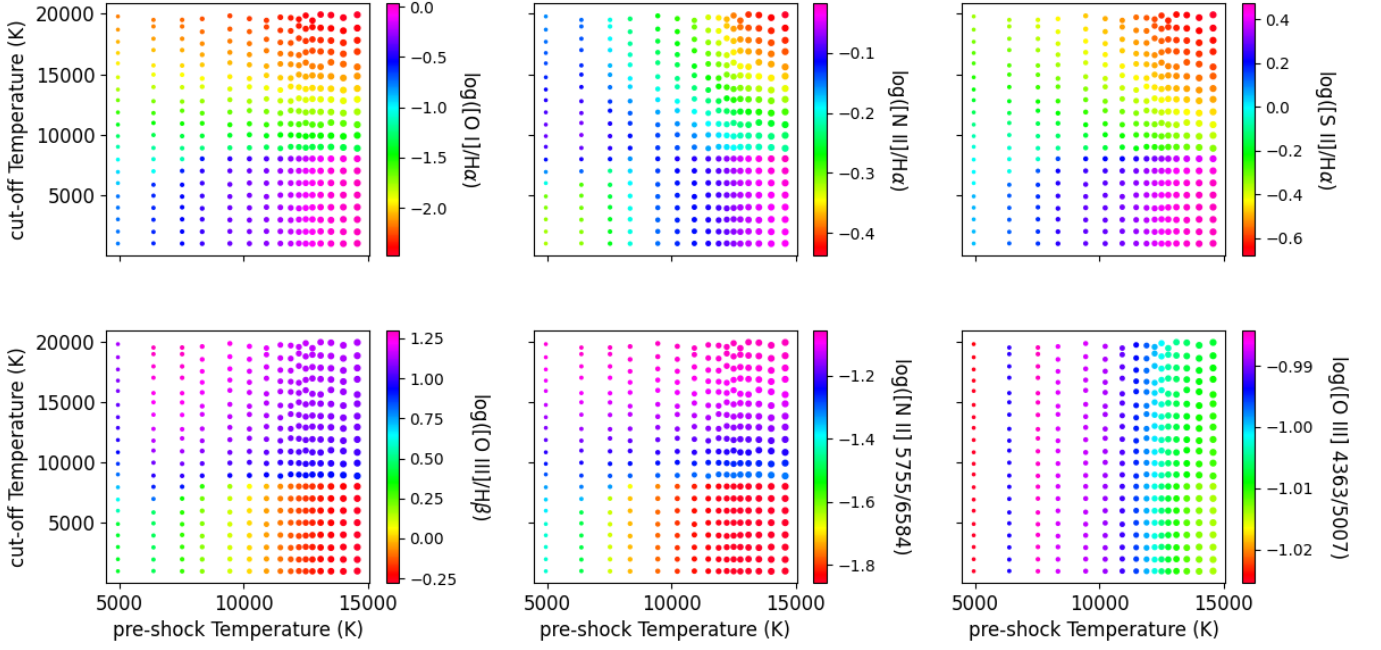
Figure B1. $T_{\text{pre-shock}}$ versus $T_{\text{cut-off}}$ plots of emission line ratios for the high velocity incomplete models (namely Allen2008_cut). The colour of the symbols correspond to the values of each line ratio and their size to the shock velocity. The larger the points, the higher the shock velocity. Only the models with shock velocity <500 km s^{-1} and pre-shock transverse magnetic fields $<0.5\mu$G are plotted.

decrease for higher magnetic field. All these changes in the line ratios with the magnetic field become readily apparent in the models with B$>4\mu$G.

It is worth to clarify that the [O III] 4363/5007 temperature diagnostic becomes as low as -1.2 (in logarithmic scale) only for high velocities models, $T_{\text{pre-shock}} \geq 13000$ K, $T_{\text{cut-off}} \leq 13000$ K and B$>4\mu$G. For the rest of the models, the [O III] 4363/5007 ratio is nearly to -1.1 .

This paper has been typeset from a TEX/LATEX file prepared by the author.